Journal of Structural Geology, Vol. 15, No. 7, pp. 923 to 932, 1993
Printed in Great Britain

0191-8141/93 $06.00+0.00

Drape folding of compressible elastic layers—II. Matrix solution for two-layer folds

WILLIAM C. HANEBERG

New Mexico Bureau of Mines and Mineral Resources, New Mexico Institute of Mining and Technology. Socorro, NM 87801, U.S.A.

(*Received* 10 *February* 1992; *accepted in revised form* 7 *September* 1992)

Abstract—A matrix solution for two-layer drape folds in compressible elastic media is used to examine the relative importance of layer compressibility, layer stiffness, and the presence or absence of lower boundary shear on fold form, principal stress direction and maximum shear stress distribution. The most obvious effect of decreasing the shear modulus of the lower layer is a change in principal stress orientation, accompanied by a decrease in maximum shear stress. Principal stress orientation, and to a lesser degree fold shape, can be further altered by changing the compressibility of an easily sheared basal layer. Characteristics of drape folds with welded and non-welded basal contacts, as observed in the field and predicted by a single-layer model of drape folding, are also further explored with the two-layer model.

INTRODUCTION

A PREVIOUS paper (Haneberg 1992), hereafter referred to as Part I, presented analytical solutions for two types of compressible elastic drape folding, which corresponded to the welded and non-welded end-members of Stearns (1978). The geologic significance of these two lower boundary conditions was discussed at some length, and will not be repeated here. An important conclusion of Part I was that details of drape fold geometry at depth, as well as the orientation of minor structures throughout the draped layer, should be controlled by the presence or absence of shear along the lower boundary. Compressibility also affected fold form to a small, but perceptible, degree. The Part I models, however, were limited to single-layer drape folds with an infinitesimally thin lower boundary. This paper extends the Part I analysis by developing a matrix solution for two-layer drape folds in compressible elastic media, so that the effects of lower boundary shear can be examined using a basal layer of finite thickness. In particular, it will be shown that the effects of variable shear across a basal layer of finite thickness are less obvious than in the single-layer folds of Part I, although the same basic patterns persist from one model to the other.

There has not been much previous work on the mechanics of multilayered drape folds. Reches & Johnson (1978) explained how to formulate the compressible elastic problem analyzed in this paper, and in general how to formulate matrix solutions to folding problems, but gave examples only for incompressible multilayers. Koch *et al.* (1981) investigated the effects of contact strength on monoclinal flexure of sedimentary sequences above laccolithic intrusions, which is a problem mechanically indistinguishable from draping over a buried fault. Their analysis was limited to stacks of simple elastic plates. Withjack *et al.* (1990) conducted a series of laboratory experiments, which subjected single and multiple clay layers to both extension and vertical displacement. However, they do not appear to have systematically evaluated the effects of an easily-sheared basal layer or contact.

TWO-LAYER MECHANICAL MODEL

General solution

The solution of plane-strain, multilayered folding problems in which axial shortening is the primary mechanism of folding has been discussed by a number of previous authors (e.g. Reches & Johnson 1978, Johnson & Pfaff 1989, Cruikshank & Johnson 1993). Each fold is assumed to be part of an infinitely long, periodic train of folds, and biharmonic solutions of the type developed in Part I are written for each layer. Then, boundary conditions are matched across each interface between layers to insure that both stresses and displacements are consistent in adjoining layers. For drape folds formed solely by vertical uplift, however, it is not necessary to include axial shortening terms, which simplifies the analysis considerably (Reches & Johnson 1978). Variables used in this analysis (Fig. 1) are the same as those

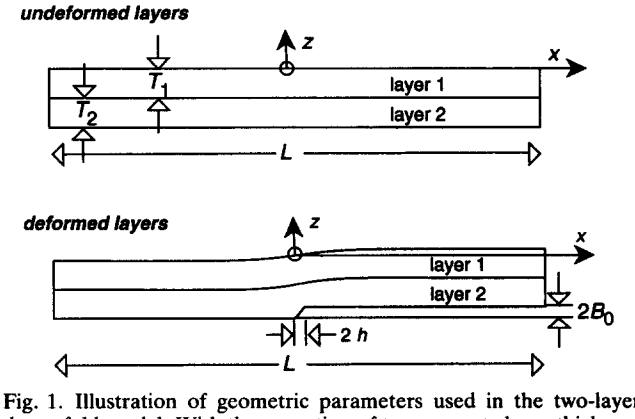

Fig. 1. Illustration of geometric parameters used in the two-layer drape-fold model. With the exception of two separate layer thickness values, these parameters are identical to those in Part I.

in Part I, except that the total thickness of the fold is the sum of two individual layer thicknesses, $T_1 + T_2$. Vertical displacement along the lower boundary is specified using a Fourier sine series, which is analogous to throw of $2B_0$ across a buried vertical fault zone of width $2h$. Neither horizontal slip along the lower boundary nor layer-parallel extension are allowed in this model. The symbolic manipulation capabilities of the computer program *Mathematica* (Wolfram 1988) were used extensively during derivation of the two-layer solution.

By analogy with Part I, the horizontal (u) and vertical (v) components of displacement within layer 1, normalized relative to the fold wavelength, L, are

$$\frac{u_1}{L} = \left[\left(\frac{c_{11}}{L} + c_{12}\frac{z}{L}\right)e^{lz} + \left(\frac{c_{13}}{L} + c_{14}\frac{z}{L}\right)e^{-lz}\right]\cos lx \quad (1)$$

$$\frac{v_1}{L} = \left\{\left[\frac{(3c_{12} - c_{11}l) + \frac{\lambda_1}{G_1}(c_{12} - c_{11}l)}{n\pi\left(1 + \frac{\lambda_1}{G_1}\right)} - c_{12}\frac{z}{L}\right]e^{lz} + \left[\frac{(3c_{14} + c_{13}l) + \frac{\lambda_1}{G_1}(c_{14} + c_{13}l)}{n\pi\left(1 + \frac{\lambda_1}{G_1}\right)} + c_{14}\frac{z}{L}\right]e^{-lz}\right\}\sin lx \quad (2)$$

and the analogous normalized components of displacement within layer 2 are

$$\frac{u_2}{L} = \left[\left(\frac{c_{21}}{L} + c_{22}\frac{z}{L}\right)e^{lz} + \left(\frac{c_{23}}{L} + c_{24}\frac{z}{L}\right)e^{-lz}\right]\cos lx \quad (3)$$

$$\frac{v_2}{L} = \left\{\left[\frac{(3c_{22} - c_{21}l) + \frac{\lambda_2}{G_2}(c_{22} - c_{21}l)}{n\pi\left(1 + \frac{\lambda_2}{G_2}\right)} - c_{12}\frac{z}{L}\right]e^{lz} + \left[\frac{(3c_{24} + c_{23}l) + \frac{\lambda_2}{G_2}(c_{24} + c_{23}l)}{n\pi\left(1 + \frac{\lambda_2}{G_2}\right)} + c_{24}\frac{z}{L}\right]e^{-lz}\right\}\sin lx. \quad (4)$$

Single subscripts represent the layer number, whereas double subscripts represent both the layer number (first subscript) and the number of the variable within that layer (second subscript). For example, c_{23} would be the third constant of integration for the second layer. The z-axis is positive upwards, and the wave number is

$$l = n\pi/L, \quad (5)$$

where n is any integer and L is the wavelength of the fold.

The layer 1 and displacement components have been multiplied throughout by $G_1/G_1 = 1$ and the layer 2 displacement components by $G_2/G_2 = 1$, which allows the four material constants of the two-layer system to be expressed in terms of three dimensionless numbers: G_2/G_1, λ_1/G_1 and λ_2/G_2. The second layer is the lowermost of the two, so values of $G_2/G_1 < 1$ mean that the lower layer is more easily sheared than is the upper layer. In terms of Young's modulus (E) and Poisson's ratio (ν), the shear modulus ratio is

$$\frac{G_2}{G_1} = \frac{E_2}{E_1}\left(\frac{1 + \nu_1}{1 + \nu_2}\right). \quad (6)$$

As in Part I, λ_1/G_1 reflects the compressibility of layer 1, or

$$\frac{\lambda_1}{G_1} = \frac{2\nu_1}{1 - 2\nu_1} \quad (7)$$

and the third material constant reflects the compressibility of layer 2, or

$$\frac{\lambda_2}{G_2} = \frac{2\nu_2}{1 - 2\nu_2}. \quad (8)$$

As before, the single subscripts denote the layer number. In practice, layer compressibilities can be specified in terms of Poisson's ratio, from which λ_1/G_1 and λ_2/G_2 can be easily calculated.

Multiplying equations (1)–(4) by L and differentiating once each with respect to x or z, as appropriate, yields the dimensionless displacement gradients

$$\frac{\partial u_1}{\partial x} = -l[(c_{11} + c_{12}z)e^{lz} + (c_{13} + c_{14}z)^{-lz}]\sin lx \quad (9)$$

$$\frac{\partial u_1}{\partial z} = \{[lc_{11} + (1 + lz)c_{12}]e^{lz} - [lc_{13} - (1 - lz)c_{14}]e^{-lz}\}\cos lx \quad (10)$$

$$\frac{\partial v_1}{\partial x} = \left\{\left[\frac{3c_{12} - c_{11}l + \frac{\lambda_1}{G_1}(c_{12} - c_{11}l)}{1 + \frac{\lambda_1}{G_1}} - c_{12}lz\right]e^{lz} + \left[\frac{3c_{14} + c_{13}l + \frac{\lambda_1}{G_1}(c_{14} + c_{13}l)}{1 + \frac{\lambda_1}{G_1}} + c_{14}lz\right]e^{-lz}\right\}\cos lx \quad (11)$$

$$\frac{\partial v_1}{\partial z} = \left\{\left[\frac{3c_{12} - c_{11}l + \frac{\lambda_1}{G_1}(c_{12} - c^{11}l)}{1 + \frac{\lambda_1}{G_1}} - (lz + 1)c_{12}\right]e^{lz} - \left[\frac{3c_{14} + c_{13}l + \frac{\lambda_1}{G_1}(c_{14} + c_{13}l)}{1 + \frac{\lambda_1}{G_1}} + (lz - 1)c_{14}\right]e^{-lz}\right\}\sin lz \quad (12)$$

$$\frac{\partial u_2}{\partial x} = -l[(c_{21} + c_{22}z)e^{lz} + (c_{23} + c_{24}z)e^{-lz}]\sin lx \quad (13)$$

$$\frac{\partial v_2}{\partial x} = \left\{\left[\frac{(3c_{22} - c_{21}l) + \frac{\lambda_2}{G_2}(c_{22} - c_{21}l)}{1 + \frac{\lambda_1}{G_2}} - c_{22}lz\right]e^{lz} + \left[\frac{(3c_{24} + c_{23}l) + \frac{\lambda_2}{G_2}(c_{24} + c_{23}l)}{1 + \frac{\lambda_2}{G_2}} + c_{24}lz\right]e^{-lz}\right\}\cos lx \quad (14)$$

$$\frac{\partial u_2}{\partial z} = \{[c_{21}l + c_{22}(1 + lz)]e^{lz} - [c_{23}l - c_{24}(1 - lz)]e^{-lz}\}\cos lx \quad (15)$$

$$\frac{\partial v_2}{\partial z} = \left\{\left[\frac{(3c_{22} - c_{21}l) + \frac{\lambda_2}{G_2}(c_{22} - c_{21}l)}{1 + \frac{\lambda_2}{G_2}} - (1 + lz)c_{22}\right]e^{lz} - \left[\frac{(3c_{24} + c_{23}l) + \frac{\lambda_2}{G_2}(c_{24} + c_{23}l)}{1 + \frac{\lambda_2}{G_2}} + (1 - lz)c_{24}\right]e^{-lz}\right\}\sin lx. \quad (16)$$

These gradients are identical in form to those in Part 1.

Once the eight displacement gradients have been evaluated, normalized stresses in each of the layers can be calculated using

$$\frac{\sigma_{xx,1}}{G_1} = \left(\frac{\lambda_1}{G_1} + 2\right)\frac{\partial u_1}{\partial x} + \frac{\lambda_1}{G_1}\frac{\partial v_1}{\partial z} \quad (17)$$

$$\frac{\sigma_{zz,1}}{G_1} = \left(\frac{\lambda_1}{G_1} + 2\right)\frac{\partial v_1}{\partial z} + \frac{\lambda_1}{G_1}\frac{\partial u_1}{\partial x} \quad (18)$$

$$\frac{\sigma_{xz,1}}{G_1} = 2\left(\frac{\partial u_1}{\partial z} + \frac{\partial v_1}{\partial x}\right) \quad (19)$$

$$\frac{\sigma_{xx,2}}{G_1} = \frac{G_2}{G_1}\left[\left(\frac{\lambda_2}{G_2} + 2\right)\frac{\partial u_2}{\partial x} + \frac{\lambda_2}{G_2}\frac{\partial v_2}{\partial z}\right] \quad (20)$$

$$\frac{\sigma_{zz,2}}{G_1} = \frac{G_2}{G_1}\left[\left(\frac{\lambda_2}{G_2} + 2\right)\frac{\partial v_2}{\partial z} + \frac{\lambda_2}{G_2}\frac{\partial u_2}{\partial x}\right] \quad (21)$$

$$\frac{\sigma_{xz,1}}{G_1} = 2\frac{G_2}{G_1}\left(\frac{\partial u_2}{\partial z} + \frac{\partial v_2}{\partial x}\right). \quad (22)$$

Tensile normal stresses are considered positive. Lithostatic normal stresses (Hafner 1951) are ignored in this analysis in order to focus attention on the perturbed stress and displacement fields that arise during folding. If desired, however, lithostatic terms can be included by simply adding them to equations (17), (18), (20) and (21).

Particular solution

In Part I, the particular solutions were found by algebraically solving four linear equations in order to determine the four constants of integration. In the two-layer model, however, there are twice as many constants of integration. Although it is possible to solve algebraically a system of eight linear equations, it is extremely impractical for folding problems. An algebraic solution to the two-layer problem was obtained using *Mathematica* (Wolfram 1988). However, the resulting expressions were several hundreds of lines long and computer limitations slowed the algebraic simplification algorithm to a crawl. In order to circumvent this difficulty, previous workers (e.g. Reches & Johnson 1978) used matrix methods to solve the equations simultaneously. This paper uses an analogous method for two compressible elastic layers, which can be expanded to model an arbitrary number of layers.

Because both layers are originally flat, the vertical normal (σ_{zz}) and horizontal shear (σ_{xz}) stresses can be used as a first-order approximation of the normal and shear stresses acting along each layer boundary. As the slopes of interfaces between drape-folded layers increase beyond about 15°, however, this approximation becomes increasingly erroneous. Similar problems are encountered in compressional or extensional folding problems, in which the interfaces separating mechanically distinct layers must have some original perturbation in order for dynamic instabilities to grow. Accuracy of the boundary stress approximations can be

increased either through higher-order algebraic approximations for slopes up to about 30° (Johnson & Pfaff 1989) or least-squares interface matching methods for high-amplitude folds (Fletcher 1974, Cruikshank & Johnson 1993).

The upper boundary of the drape fold is assumed to be traction free, subjected to neither shear nor normal forces. This corresponds to the Earth's surface. Mathematically, the first two boundary conditions are:

$$\sigma_{xz,1} = 0 \tag{23}$$

$$\sigma_{zz,1} = 0 \tag{24}$$

evaluated at $z = 0$. In order that the contact between the two elastic layers does not separate during folding, layer-parallel and layer-perpendicular displacements and stresses must be equal in both layers. This gives the four internal boundary conditions

$$\sigma_{xz,1} = \sigma_{xz,2} \tag{25}$$

$$\sigma_{zz,1} = \sigma_{zz,2} \tag{26}$$

$$u_1 = u_2 \tag{27}$$

$$v_1 = v_2 \tag{28}$$

evaluated along the undeformed contact, which is given by the Lagrangian co-ordinate $z = -T_1$.

Boundary condition (25) implies that the contact between the two compressible layers is strongly bonded, so that no slip can occur along the interface between the two layers. Instead, layer-parallel displacement with the lower portion of the two-layer fold can be simulated by reducing the shear modulus of layer 2. This combination of a no-slip boundary condition and an easily sheared lower layer distributes shear throughout layer 2, which has finite thickness, rather than along an infinitesimally thin contact as in Part I. In this manner, conclusions about the importance of basal shear on fold form and minor structures can be more fully examined. If free slip between the two layers were desired, however, equation (25) could be re-written as $\sigma_{xz,1} = 0$ and $\sigma_{xz,2} = 0$. Finally, the base of layer 2 is subjected to the same displacement conditions as in Case I of Part I

$$u_2 = 0 \tag{29}$$

$$\frac{v_2}{L} = b_n \sin lx \tag{30}$$

evaluated at $z = -(T_1 + T_2)$. Thus, there is no slip allowed along the base of layer 2. The Fourier coefficients in (30) are given by

$$b_n = \frac{2B_0/L}{n\pi - 4n^3\pi(h/L)^2}\left[\cos\left(n\pi\frac{h}{L}\right) - \left(\left\{1 - 4n^2\left(\frac{h}{L}\right)^2 \times \left[1 - \cos\left(\frac{\pi}{2}\frac{L}{h}\right)\right]\right\}\cos\left(n\pi\frac{h}{L}\right) - \left[4n^2\left(\frac{h}{L}\right)^2 - 2n\left(\frac{h}{L}\right)\sin\left(n\pi\frac{h}{L}\right)\right]\sin\left(\frac{\pi}{2}\frac{L}{h}\right)\right)(-1)^n\right] \tag{31}$$

which is identical to that used in Part I. As before, any Fourier sine series could have been used to specify vertical displacement along the base of layer 2.

Each of the boundary conditions is evaluated by substituting the appropriate stress or displacement equation(s) into equations (23)–(30), and setting z equal to 0, $-T_1$, or $-(T_1 + T_2)$ as appropriate. This will give rise to eight linear equations that can be rearranged and put into the matrix form

$$\mathbf{Mc} = \mathbf{f}$$

or, expanding the boundary condition equations,

$$\begin{bmatrix} 0 & m_{12} & 0 & m_{14} & 0 & 0 & 0 & 0 \\ m_{21} & m_{22} & m_{23} & m_{24} & 0 & 0 & 0 & 0 \\ 0 & m_{32} & 0 & m_{34} & 0 & m_{36} & 0 & m_{38} \\ m_{41} & m_{42} & m_{43} & m_{44} & m_{45} & m_{46} & m_{47} & m_{48} \\ m_{51} & m_{52} & m_{53} & m_{54} & m_{55} & m_{56} & m_{57} & m_{58} \\ m_{61} & m_{62} & m_{63} & m_{64} & m_{65} & m_{66} & m_{67} & m_{68} \\ 0 & 0 & 0 & 0 & m_{75} & m_{76} & m_{77} & m_{78} \\ 0 & 0 & 0 & 0 & m_{85} & m_{86} & m_{87} & m_{88} \end{bmatrix} \begin{Bmatrix} c_{11} \\ c_{12} \\ c_{13} \\ c_{14} \\ c_{21} \\ c_{22} \\ c_{23} \\ c_{24} \end{Bmatrix} = \begin{Bmatrix} 0 \\ 0 \\ 0 \\ 0 \\ 0 \\ 0 \\ 0 \\ b_n \end{Bmatrix}. \tag{32}$$

This system of eight equations must be solved repeatedly for many values of n (in this paper $n = 1 \ldots 100$), and the results added together to arrive at an adequate approximation of the desired boundary displacement. The 42 non-zero elements of **M** are listed in the Appendix.

Drawing an analogy from the vocabulary of structural engineering, **M** is the stiffness matrix, which takes into account the material properties and thicknesses of the layers. Likewise, **f** is the driving vector, which characterizes the width of and throw across a buried vertical fault. In this problem, vertical uplift along the base of layer 2 is the sole component of the driving vector.

The coefficient vector **c** can be calculated using one of the linear equation solvers available in most mathematical subroutine packages. There are, however, two caveats. First, the method of solution must employ some form of pivoting because, as the problem is formulated in this paper, the diagonal elements m_{11} and m_{33} are zero. Second, the stiffness matrix **M** tends to be highly ill-conditioned. This means that small changes in the driving vector **f** will produce large changes in the coefficient vector **c**. In order to circumvent potential conditioning problems, the examples presented in this paper were solved using L–U decomposition and back-substitution with iterative improvement (Press *et al.* 1988).

RESULTS

The effects of contrasting layer stiffness and layer compressibility can be illustrated using the series of four examples summarized in Table 1. The objective of these numerical experiments is to investigate the transition from a welded to a non-welded contact (Stearns 1978) by varying the stiffness and compressibility along the base of a theoretical drape fold. In Part I, Case I corresponded to a welded contact along which no layer-

Table 1. Geometry and material constants for Examples 1–4

Example	T_1/L	T_2/L	B_0/L	h/L	G_2/G_1	ν_1	ν_2
1	0.05	0.05	0.01	0.01	1.00	0.10	0.10
2	0.05	0.05	0.01	0.01	0.10	0.10	0.10
3	0.05	0.05	0.01	0.01	0.10	0.10	0.25
4	0.05	0.05	0.01	0.01	0.10	0.10	0.49

parallel slip was allowed and Case 2 corresponded to a non-welded contact with no shear strength. Example 1, in which neither stiffness or rigidity vary between the two layers, is identical to a Case I fold of thickness $T/L = 0.10$ in Part I. In the other three examples, the stiffness and compressibility contrast between the two layers is varied. Layer thickness, fault zone width and vertical displacement along the lower boundary are held constant in all four examples. The model results are presented in four ways: fold form; displacement field; principal stress trajectory field; and maximum shear stress field. The first three categories are familiar to geologists; however, because tensile stresses are defined as positive, the greatest principal stress (σ_1) is the most tensile or least compressive principal stress. Likewise, σ_3 is the most compressive or least tensile principal stress.

For the examples given below, maximum shear stress (e.g. Pollard & Segall 1987) values were calculated on a grid of 21 rows × 201 columns, and the values from four grid points were used to calculated an average value for each of 4000 quadrilaterals. Average values mask both the highest and lowest point values associated with each quadrilateral; however, the maximum and minimum calculated values are given along the scale bar beneath each shear stress plot. The displacement solutions derived above were used to transform each originally square element into its deformed shape, allowing the average maximum shear stress within each deformed quadrilateral to be plotted as part of a gray-scale diagram.

When there is no stiffness or compressibility contrast between layers, the two-layer solution (Fig. 2) produces results identical to the Case I single layer solution (Part I).

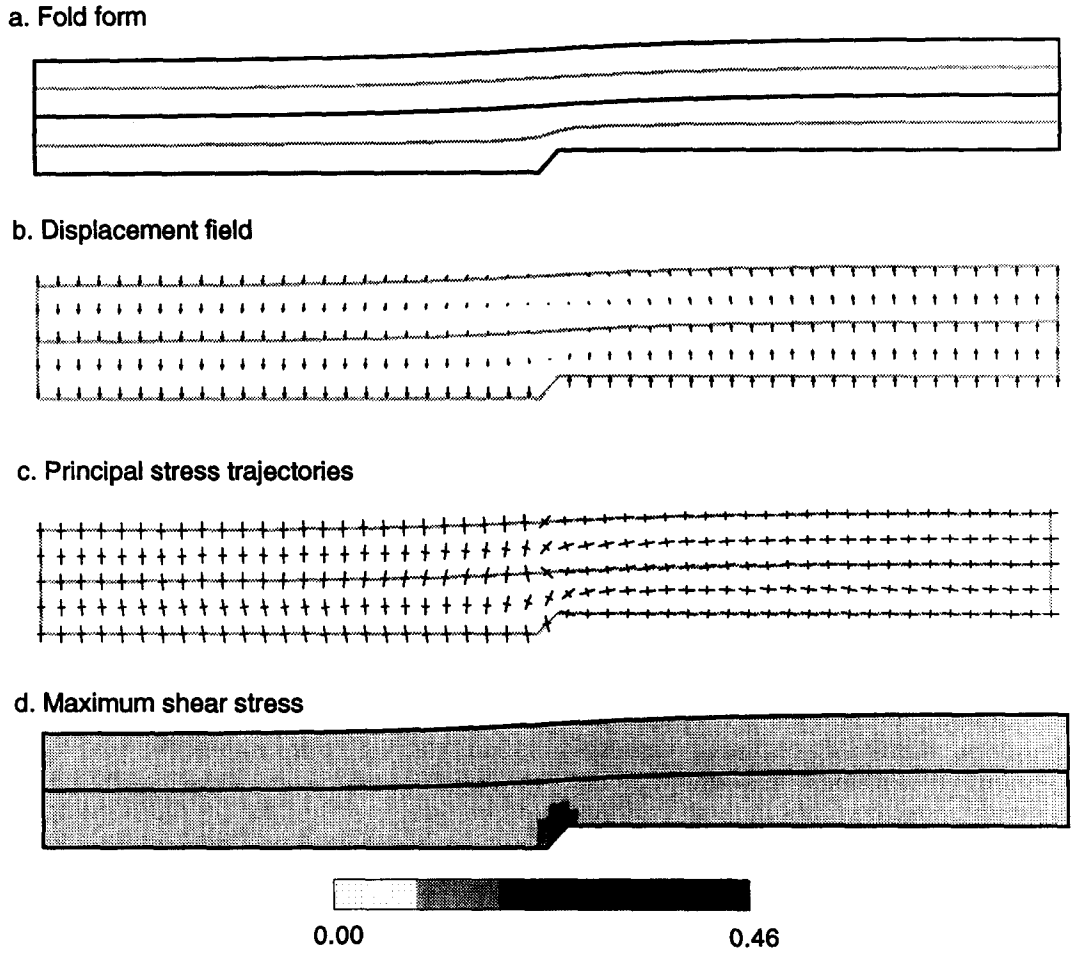

Fig. 2. Results of Example 1, which is identical to a Case I (welded base) fold of thickness $T/L = 0.1$ in Part I. (a) Fold form, with black lines used to denote the two layers, and gray lines used to denote passive markers within each of the layers. The passive markers are kinematic indicators that deform with the layer but have no mechanical effect. (b) Displacement field, showing resultant vectors ($\sqrt{u^2 + v^2}$). Outlines of the two layers are shown in the background. (c) Principal stress trajectory field. Long axes represent the most tensile principal stress (σ_1), whereas short axes represent the most compressive principal stress (σ_3). Outlines of the two layers are shown in the background. (d) Averaged maximum shear stress intensity, with minimum and maximum values indicated on the scale bar. No horizontal or vertical exaggeration in any of the figures.

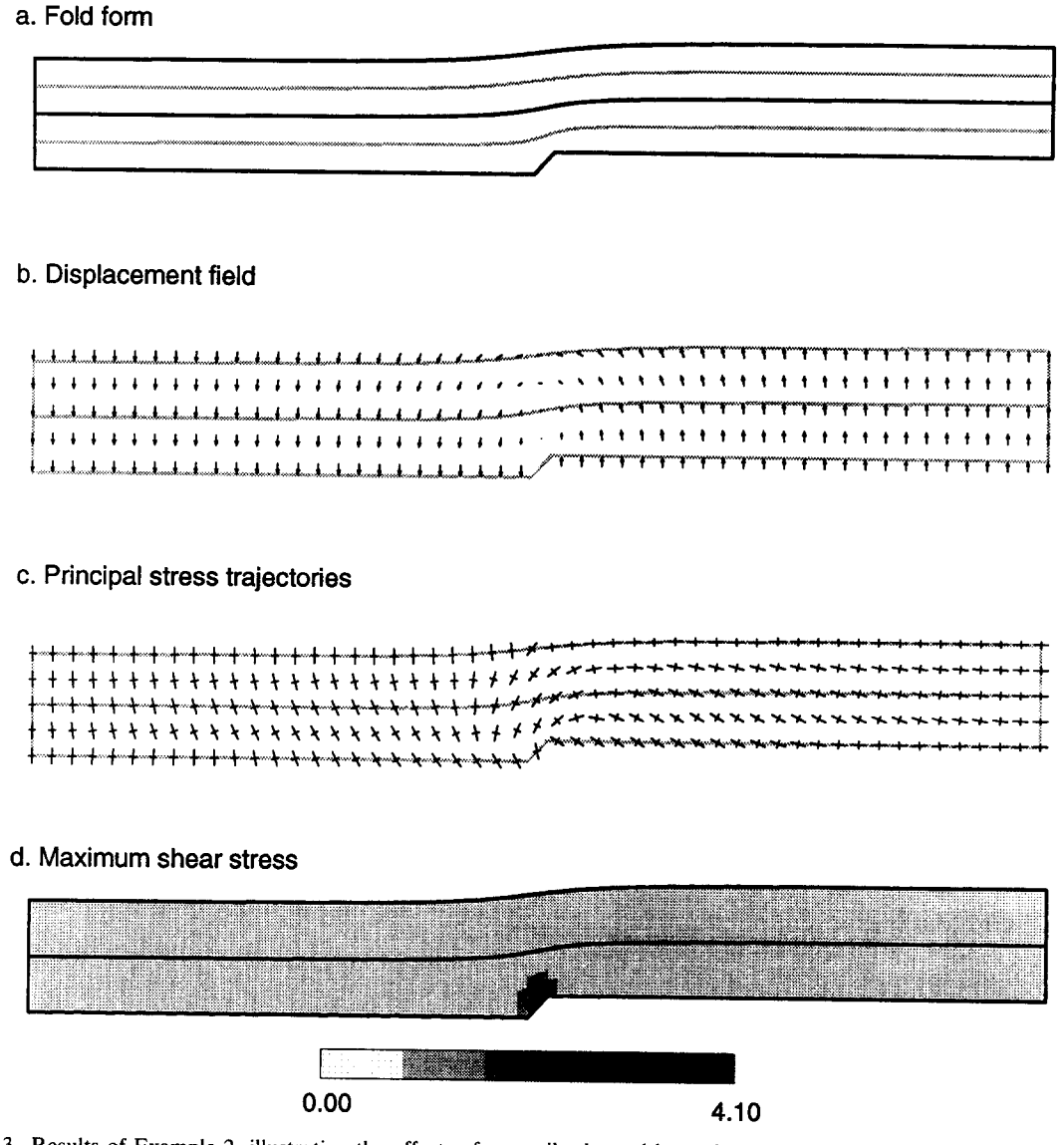

Fig. 3. Results of Example 2, illustrating the effects of an easily-sheared lower layer with no compressibility contrast. Explanations for parts (a)–(d) are the same as in Fig. 2, and material constants shown in Table 1.

When the stiffness of the lower layer is reduced by an order of magnitude, however, subtle changes begin to occur (Fig. 3). There is essentially no difference in the forms of Example 1 and Example 2 folds; however, the resultant displacement vectors in layer 2 of Fig. 3 are directed slightly inward. For comparison with the two end-members developed in Part I, this is the beginning of a transformation from the distinctly concave-downward, ∩-shaped displacement field characteristic of Case I folds to the concave-upward, ∪-shaped displacement characteristic of Case II folds. Stress trajectories are more nearly parallel to the interface between layers 1 and 2 than in Example 1 (Fig. 2) stress trajectories, because shear stresses along the interface are approaching zero. The maximum shear stress also drops nearly an order of magnitude, from $4.10G_1$ to $0.46G_1$, between Example 1 and Example 2. In both cases, however, elevated shear stresses are concentrated directly above the fault scarp.

Example 3 (Fig. 4) is an intermediate case included to illustrate the relative insensitivity of the model to small changes in layer compressibility. The stiffness contrast between the two layers remains at $G_2/G_1 = 0.1$, but the Poisson's ratio of layer 2 is increased from $\nu_2 = 0.10$ to $\nu_2 = 0.25$. There are two effects. First, there is a barely perceptible tilting of principal stress axes within and along the boundaries of layer 2. This tilting is best observed by overlaying enlargements of Figs. 3(c) and 4(c) on a light table or computer screen. Again recalling the definition of principal stress planes, the small degree of rotation from horizontal and vertical means that layer-parallel shear stress is increasing within layer 2, and is also being transferred to layer 1. The second effect is a small increase in maximum shear stress from $0.46G_1$ in Example 2 to $0.58G_1$ in Example 3.

Much more noticeable changes occur if the lower layer is given a Poisson's ratio of $\nu_2 = 0.49$, making it essentially incompressible (Fig. 5). First, the drape fold becomes tighter, particularly through the upper layer. Second, the ∪-shaped displacement vector field becomes even more strongly developed. Third, principal stress axes along the boundaries of layer 2 are rotated

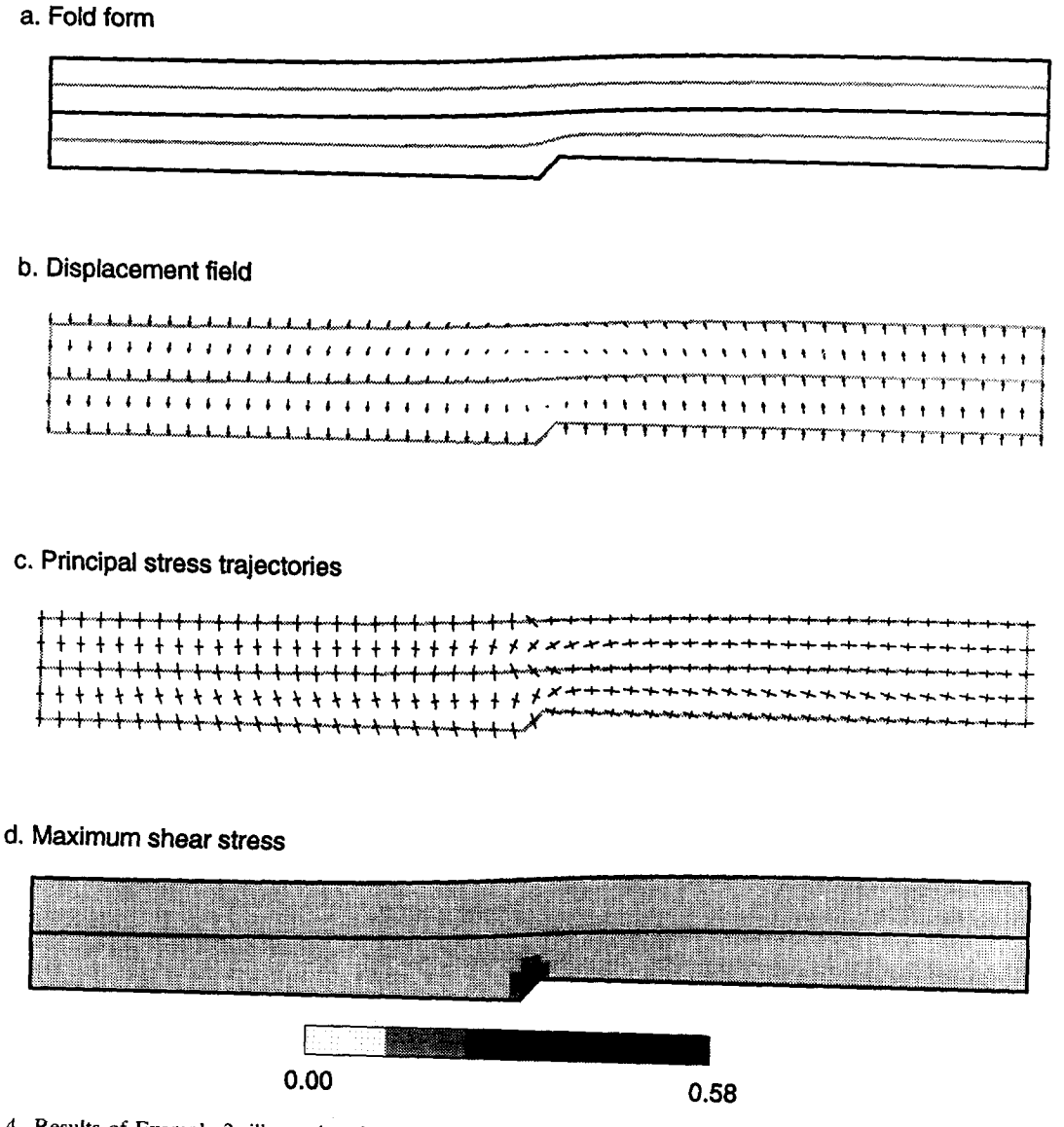

Fig. 4. Results of Example 3, illustrating the effects of an easily-sheared lower layer with a moderate compressibility contrast. Explanations for parts (a)–(d) are the same as in Fig. 2, and material constants shown in Table 1.

approximately 45° from horizontal and vertical. Principal stress orientation within layer 2 is also highly variable. Notice that, on the left-hand side of Fig. 5(c), the state of stress within layer 2 changes from layer-parallel deviatoric compression near the underlying fault to layer-parallel deviatoric tension away from the underlying fault. The reverse is true on the right-hand side of Fig. 5(c). Fourth, the maximum shear stress increases slightly, from $0.58G_1$ in Example 3 to $0.72G_1$ in Example 4, and a small zone of elevated shear stress begins to develop near the base of layer 1.

One of the major conclusions of Part I was that nonwelded (Case II) lower boundaries should become asymmetric during draping, and that the inflection point of the lower boundary should shift slightly towards the upthrown side of the fault. The gradual development of concave-upward, or U-shaped displacement fields in Examples 2–4 shows that the same asymmetry develops, albeit much more weakly, in two-layer drape folds with easily sheared lower layers. The asymmetry is emphasized by a plot showing the curvature, or second derivative, of the height of the deformed interface $(z + v)$ with respect to the final horizontal co-ordinates $(x + u)$, of the passive marker within layer 2 (Fig. 6). Large absolute values indicate tight folds, whereas small absolute values indicate open folds; positive values reflect concave-upward curvature, whereas negative values indicate concave-downward curvature. In Example 1, both the positive and negative peaks have approximately the same width and amplitude. This means that the deformed passive marker developed sinusoidal symmetry during deformation. In Example 4, however, the concave-upward portion of the drape fold is wider and more open than the concave-downward portion, just as in Case II of Part I. In addition, the entire Example 4 curve is shifted slightly to the right.

DISCUSSION

A series of numerical experiments shows that the distinctive end-member characteristics of drape folds

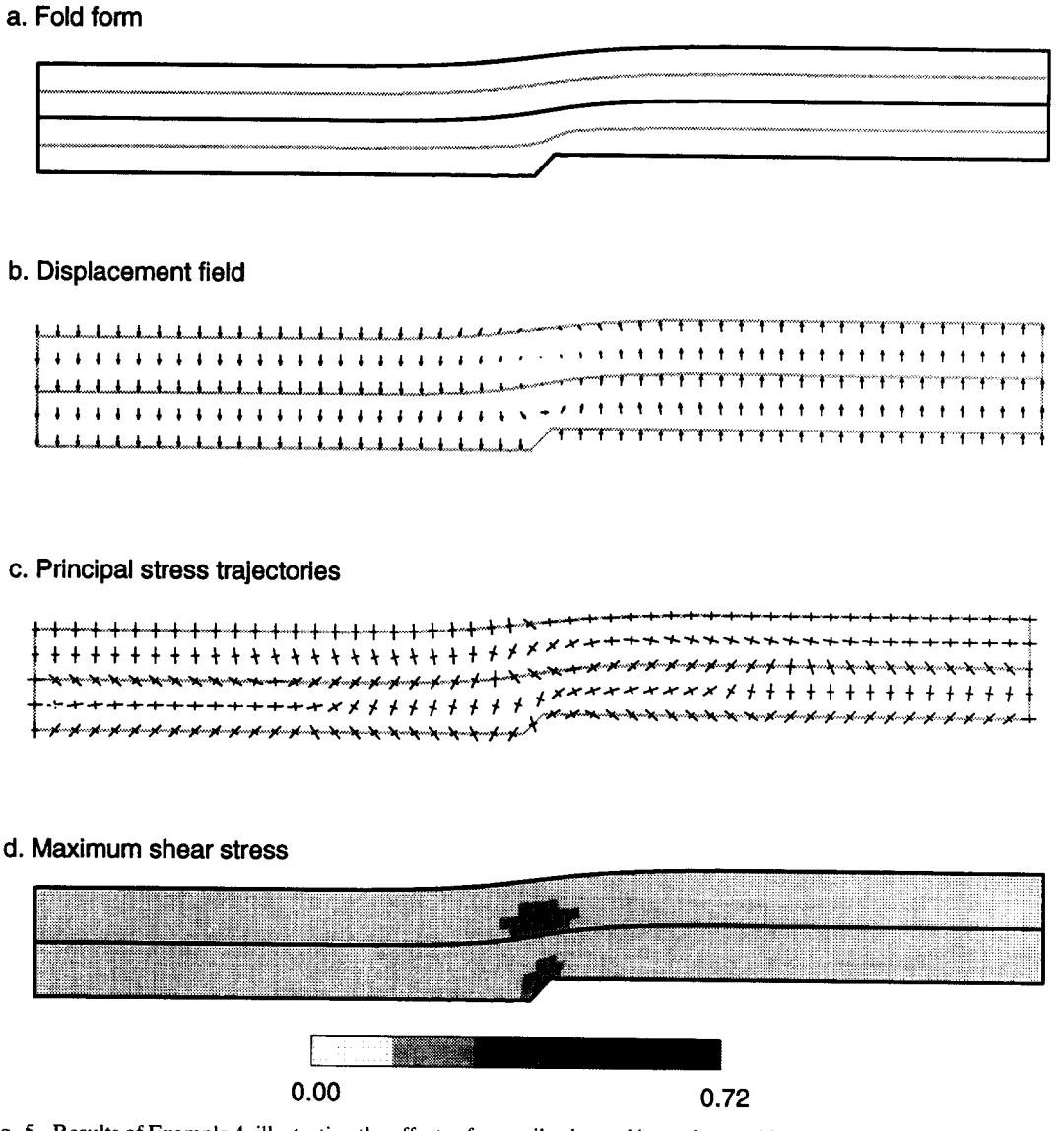

Fig. 5. Results of Example 4, illustrating the effects of an easily-sheared lower layer with a strong compressibility contrast. Explanations for parts (a)–(d) are the same as in Fig. 2, and material constants shown in Table 1.

with welded and non-welded bases, described previously in Part I, can be qualitatively reproduced using a two-layer mechanical model with an easily sheared, nearly incompressible base. These characteristics, however, are not as strongly developed as in Part I. This may be because the basal contact in Case II of Part I was infinitesimally thin, perfectly frictionless and perfectly incompressible. The present analysis, in contrast, treats a basal layer of finite thickness with a finite shear modulus and some compressibility. The effects of large vertical displacement and layer parallel extension, which have been investigated in the laboratory by others (e.g. Withjack *et al.* 1990), remain uncertain.

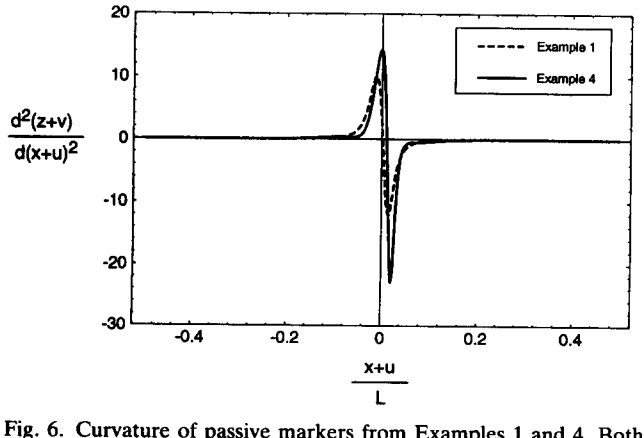

Fig. 6. Curvature of passive markers from Examples 1 and 4. Both markers were originally straight lines at a depth of $z/L = -0.075$. The asymmetry of the drape-folded markers is indicated by the markedly asymmetric curvature of the Example 4 marker.

Whereas the effects of a weak basal layer could have been predicted to some degree from the results of Part I, the effects of a compressibility contrast were not evident in the single layer solution. At the very least, this analysis shows that compressibility contrasts can produce noticeable changes in stress orientation and magnitude, as well as small changes in fold form (cf. Reches & Johnson 1978). Geologically, then, it might be important to distinguish between slow and rapid deformation of a saturated clay or shale. If deformation were slow, excess pore pressures might be quickly dissipated and the hypothetical saturated layer would become effectively very compressible. If the deformation were rapid,

on the other hand, then the saturated layer would become very nearly incompressible. In the parlance of soil mechanics and modern poroelastic theory (e.g Rice & Cleary 1976), these two modes of deformation correspond to drained and undrained loading.

The four examples given here suggest that one might, in principle, be able to infer both stiffness and compressibility contrasts by careful mapping of minor structures or strain distributions in real folds. To wit, the only difference between Examples 2, 3 and 4 is the compressibility of the lower layer. Although there is little perceptible difference between the idealized elastic layers in Examples 2 and 3, there is a noticeable difference between either of these two and Example 4. Whether or not the differences will be significant enough to be discernable in rocks is another matter, although it has been shown that careful analysis of mechanical stratigraphy can be used to successfully model the general forms of real folds (Johnson & Pfaff 1989, Cruikshank & Johnson 1993). The complicated inter-relationships among geometry, stiffness and compressibility, however, suggest that oversimplified attempts to infer details of subsurface structure from the surface expression of a fold may be prone to failure. Each additional layer confounds the problem of subsurface prediction, which was first raised with regard to single-layer drape folds in Part I.

Acknowledgements—This work was supported primarily by the New Mexico Bureau of Mines and Mineral Resources, with additional funding from the United States Geological Survey through the New Mexico Water Resources Research Institute (grant 01423954). Discussions with K. M. Cruikshank help to clarify some mechanical issues, and comments by A. M. Johnson and an anonymous reviewer improved the manuscript. An unpublished manuscript by A. M. Johnson and R. C. Fletcher, "Theories of Folding and Density Instability", was also invaluable during this work.

REFERENCES

Cruikshank, K. M. & Johnson, A. M. 1993. High-amplitude folding of linear-viscous multilayers. *J. Struct. Geol.* **15**, 79–94.

Fletcher, R. C. 1974. Wavelength selection in the folding of a single layer with power-law rheology. *Am. J. Sci.* **274**, 1029–1043.

Hafner, W. 1951. Stress distributions and faulting. *Bull. geol. Soc. Am.* **62**, 373–398.

Haneberg, W. C. 1992. Drape folding of compressible elastic layers—I. Analytical solutions for vertical uplift. *J. Struct. Geol.* **14**, 713–721.

Johnson, A. M. & Pfaff, V. J. 1989. Parallel, similar and constrained folds. In: Richard H. Jahns Memorial Volume (edited by Johnson A. M., Burnham, C. W., Allen, C. R., & Muehlberger, W.). *Engng Geol.* **27**, 115–180.

Koch, F. G., Johnson, A. M. & Pollard, D., D. 1981. Monoclinal bending of strata over laccolithic intrusions. *Tectonophysics* **74**, T21–T31.

Pollard, D. D. & Segall, P. 1987. Theoretical displacements and stresses near fractures in rock: with applications to faults, joints, veins, dikes, and solution surfaces. In: *Fracture Mechanics of Rock* (edited by Atkinson, B. K.). Academic Press, London, 277–349.

Press, W. H., Flannery, B. P., Teukolsky, S. A. & Vetterling, W. T. 1988. *Numerical Recipes in C*. Cambridge University Press, Cambridge.

Reches, Z. & Johnson, A. M. 1978. Development of monoclines: Part II. Theoretical analysis of monoclines. In: *Laramide Folding Associated with Basement Block Faulting in the Western United States* (edited by Matthews, V., III). *Mem. geol. Soc. Am.* **151**, 273–312.

Rice, J. R. & Cleary, M. P. 1976. Some basic stress solutions for fluid-saturated porous media with compressible constitutents. *Rev. Geophys. & Space Phys.* **14**, 227–241.

Stearns, D. W. 1978. Faulting and forced folding in the Rocky Mountains foreland. In: *Laramide Folding Associated with Basement Block Faulting in the Western United States* (edited by Matthews, V., III). *Mem. geol. Soc. Am.* **151**, 1–37.

Withjack, M. O., Olson, J. & Peterson, E. 1990. Experimental models of extensional forced folds. *Bull. Am. Ass. Petrol. Geol.* **74**, 1038–1054.

Wolfram, S. 1988. *Mathematica*. Addison-Wesley, Redwood City, California.

APPENDIX

Elements of the stiffness matrix **M** are found by evalutating the two upper, four internal, and two lower boundary conditions at $z/L = 0$, $z/L = -T_1$ and $z/L = -(T_1 + T_2)$, respectively. Terms in each of the eight boundary condition equations are then grouped in order to isolate the coefficients of $c_{11} \ldots c_{24}$. The 42 non-zero elements of **M** are:

$$m_{12} = 4\left(\frac{2+\frac{\lambda_1}{G_1}}{1+\frac{\lambda_1}{G_1}}\right) \tag{A1}$$

$$m_{14} = m_{12} \tag{A2}$$

$$m_{21} = -2l\left(1+\frac{\lambda_1}{G_1}\right) \tag{A3}$$

$$m_{22} = \tfrac{1}{2}m_{12} \tag{A4}$$

$$m_{23} = m_{21} \tag{A5}$$

$$m_{24} = -m_{22} \tag{A6}$$

$$m_{32} = m_{12}e^{-lT_1} \tag{A7}$$

$$m_{34} = m_{12}e^{lT_1} \tag{A8}$$

$$m_{36} = 4\frac{G_2}{G_1}\left(\frac{2+\frac{\lambda_2}{G_2}}{1+\frac{\lambda_2}{G_2}}\right)e^{-lT_1} \tag{A9}$$

$$m_{38} = 4\frac{G_2}{G_1}\left(\frac{2+\frac{\lambda_2}{G_2}}{1+\frac{\lambda_2}{G_2}}\right)e^{lT_1} \tag{A10}$$

$$m_{41} = m_{21}e^{-lT_1} \tag{A11}$$

$$m_{42} = 2\left[\frac{2+lT_1+\frac{\lambda_1}{G_1}+2lT_1\frac{\lambda_1}{G_1}+lT_1\left(\frac{\lambda_1}{G_1}\right)^2}{1+\frac{\lambda_1}{G_1}}\right]e^{-lT_1} \tag{A12}$$

$$m_{43} = m_{21}e^{lT_1} \tag{A13}$$

$$m_{44} = 2\left[\frac{-2+lT_1-\frac{\lambda_1}{G_1}+2lT_1\frac{\lambda_1}{G_1}+lT_1\left(\frac{\lambda_1}{G_1}\right)^2}{1+\frac{\lambda_1}{G_1}}\right]e^{lT_1} \tag{A14}$$

$$m_{45} = 2l\frac{G_2}{G_1}\left(1+\frac{\lambda_2}{G_2}\right)e^{-lT_1} \tag{A15}$$

$$m_{46} = -2\frac{G_2}{G_1}\left[\frac{2+\frac{\lambda_2}{G_2}+lT_1+2lT_1\frac{\lambda_2}{G_2}+lT_1\left(\frac{\lambda_2}{G_2}\right)^2}{1+\frac{\lambda_2}{G_2}}\right]e^{-lT_1} \tag{A16}$$

$$m_{47} = 2l\frac{G_2}{G_1}\left(1 + \frac{\lambda_2}{G_2}\right)e^{lT_1} \tag{A17}$$

$$m_{48} = 2\frac{G_2}{G_1}\left[\frac{2 + \frac{\lambda_2}{G_2} - lT_1 - 2lT_1\frac{\lambda_2}{G_2} - lT_1\left(\frac{\lambda_2}{G_2}\right)^2}{1 + \frac{\lambda_2}{G_2}}\right]e^{lT_1} \tag{A18}$$

$$m_{51} = e^{-lT_1} \tag{A19}$$

$$m_{52} = -T_1 m_{51} \tag{A20}$$

$$m_{53} = e^{lT_1} \tag{A21}$$

$$m_{54} = -T_1 m_{53} \tag{A22}$$

$$m_{55} = -m_{51} \tag{A23}$$

$$m_{56} = -m_{52} \tag{A24}$$

$$m_{57} = -m_{53} \tag{A25}$$

$$m_{58} = -m_{54} \tag{A26}$$

$$m_{61} = m_{55} \tag{A27}$$

$$m_{62} = \left[\frac{3 + lT_1 + \frac{\lambda_1}{G_1} + lT_1\frac{\lambda_1}{G_1}}{l\left(1 + \frac{\lambda_1}{G_1}\right)}\right]e^{-lT_1} \tag{A28}$$

$$m_{63} = m_{53} \tag{A29}$$

$$m_{64} = \left[\frac{3 - lT_1 + \frac{\lambda_1}{G_1} - lT_1\frac{\lambda_1}{G_1}}{l\left(1 + \frac{\lambda_1}{G_1}\right)}\right]e^{lT_1} \tag{A30}$$

$$m_{65} = m_{51} \tag{A31}$$

$$m_{66} = -\left[\frac{3 + \frac{\lambda_2}{G_2} + lT_1 - lT_1\frac{\lambda_2}{G_2}}{l\left(1 + \frac{\lambda_2}{G_2}\right)}\right]e^{-lT_1} \tag{A32}$$

$$m_{67} = m_{57} \tag{A33}$$

$$m_{68} = \left[\frac{-3 - \frac{\lambda_2}{G_2} + lT_1 + lT_1\frac{\lambda_2}{G_2}}{l\left(1 + \frac{\lambda_2}{G_2}\right)}\right]e^{lT_1} \tag{A34}$$

$$m_{75} = e^{-l(T_1+T_2)} \tag{A35}$$

$$m_{76} = -(T_1 + T_2)m_{75} \tag{A36}$$

$$m_{77} = e^{l(T_1+T_2)} \tag{A37}$$

$$m_{78} = -(T_1 + T_2)m_{77} \tag{A38}$$

$$m_{85} = -m_{75} \tag{A39}$$

$$m_{86} = \left[\frac{3 + \frac{\lambda_2}{G_2} + l(T_1 + T_2) + l(T_1 + T_2)\frac{\lambda_2}{G_2}}{l\left(1 + \frac{\lambda_2}{G_2}\right)}\right]e^{-l(T_1+T_2)} \tag{A40}$$

$$m_{87} = m_{77} \tag{A41}$$

$$m_{88} = \left[\frac{3 + \frac{\lambda_2}{G_2} + l(T_1 + T_2) + l(T_1 + T_2)\frac{\lambda_2}{G_2}}{l\left(1 + \frac{\lambda_2}{G_2}\right)}\right]e^{l(T_1+T_2)}. \tag{A42}$$